Surface & Coatings Technology 397 (2020) 126005

Contents lists available at ScienceDirect

Surface & Coatings Technology

journal homepage: www.elsevier.com/locate/surfcoat

Soapstone reinforced hydroxyapatite coatings for biomedical applications

Laureana Moreira Mota[a], Daniel Nilson Nunes Nicomedes[a], Ana Paula Moreira Barboza[a], Sérgio Luís Lima de Moraes Ramos[b], Rebecca Vasconcellos[c], Nathanael Vieira Medrado[c], Érika Costa de Alvarenga[c,d], Giovanna Machado[e], Karyne R.C. Juste[f], Cláudia Karina de Vasconcelos[g,j], Ariete Righi[h], Sara Matte Manhabosco[i], Rodrigo Ribeiro Resende[c], Ronaldo Junio Campos Batista[a], Jaqueline dos Santos Soares[a], Taíse Matte Manhabosco[a,*]

[a] Departamento de Física, Universidade Federal de Ouro Preto, Campus Universitário Morro do Cruzeiro ICEB/DEFIS, 35400-000 Ouro Preto, Minas Gerais, Brazil
[b] Centro de Tecnologia em Nanomateriais e Grafeno (CTNano), Universidade Federal de Minas Gerais, 31270-901 Belo Horizonte, Minas Gerais, Brazil
[c] Departamento de Bioquímica e Imunologia, Instituto de Ciência Biológicas, Universidade Federal de Minas Gerais, Laboratório de Sinalização celular e Nanobiotecnologia, Av. Antônio Carlos 6627, 31270-901 Belo Horizonte, Minas Gerais, Brazil
[d] Departamento de Ciências Naturais, Universidade Federal de São João Del Rei, Preça Dom Helvécio 74, 36301-160 São João del Rei, Minas Gerais, Brazil
[e] Centro de Tecnologias Estratégicas do Nordeste-CETENE, Av. Prof. Luiz Freire 01, 50740-540 Recife, Brazil
[f] Instituto SENAI de Inovação em Engenharia de Superfícies, Rua Sete 2000, Bairro Horto Florestal, 31035-536 Belo Horizonte, Minas Gerais, Brazil
[g] Departamento de Física e Química, Pontifícia Universidade Católica de Minas Gerais, Av. Dom José Gaspar 500, 30.535-901 Belo Horizonte, Minas Gerais, Brazil
[h] Departamento de Física, Universidade Federal de Minas Gerais, 31270-901 Belo Horizonte, Minas Gerais, Brazil
[i] Laboratório de Metrologia, Universidade Federal do Rio Grande, Campus Carreiros, Av. Itália, km 8, 96203-900, Rio Grande, Rio Grande do Sul, Brazil
[j] Departamento de Engenharia Química, Pontifícia Universidade Católica de Minas Gerais, Av. Dom José Gaspar 500, 30.535-901 Belo Horizonte, Minas Gerais, Brazil

ARTICLE INFO

Keywords:
Soapstone talc
Pulsed electrodeposition
Hydroxyapatite
Biocompatibility

ABSTRACT

Mechanical resistant bioactive materials are of high interest for biomedical applications. In this work, we address the improvement in mechanical properties of HA coatings by the addition of a cheap and widely available secondary phase material, the talc from soapstone. The composites hydroxyapatite/talc (HA/talc) were successfully obtained by pulsed electrodeposition and characterized by scanning electron microscopy, energy-dispersive X-ray spectroscopy, Raman spectroscopy, corrosion and wear resistance and biocompatibility tests. We found that the addition of talc greatly improves the mechanical properties of coatings (i. e., wear track and friction coefficient in wear tests were significantly diminished) without diminishing corrosion resistance and biocompatibility. Alamar Blue® tests, alkaline phosphatase activity, and collagen production indicate that the biocomposites are biocompatible and talc itself induce bone maturation.

1. Introduction

The so-called biomaterials are natural or synthetic materials suitable to work inside the human body, where they are employed in devices such as artificial joints and dental implants. To be inserted into the human body materials must: (*i*) be non-toxic; (*ii*) not corrode or degrade once they are inside the body; (*iii*) be stable during implantation process; (*iv*) be non-carcinogenic; and (*v*), present suitable mechanical properties, e.g., high resistance to wear and tenacity. Among biomaterials, those classified as bioactive are of special interest. Bioactive materials are those materials that, once inside the human body, interact with the surrounding tissue, either bones or soft tissue, promoting a beneficial effect. For instance, it has already been shown that a bioactive silicate-based ceramic material can bind to bone tissue after being implanted, promoting osseointegration [1]. Other major examples of bioactive materials are synthetic hydroxyapatite, glass-ceramic A-W, and Bioglass. In common, all those materials have the disadvantage of being fragile, a characteristic that prevents their use in orthopedic prosthesis and dental implants, for instance. Therefore, the study of bioactive materials with suitable mechanical properties (such as fatigue resistance, wear-resistance, and tenacity) is of high interest.

In the last decades, advances in nanoscience and nanotechnology have allowed the control of matter at the nanometric scale, which leads to modifications in the macroscopic properties of materials. In particular, one can cite the improvement of the tenacity of a fragile ceramic material through the incorporation of bidimensional nanomaterials,

* Corresponding author.
E-mail address: taise@ufop.edu.br (T. Matte Manhabosco).

https://doi.org/10.1016/j.surfcoat.2020.126005
Received 20 April 2020; Received in revised form 31 May 2020; Accepted 1 June 2020
Available online 03 June 2020
0257-8972/

like graphene oxide, in the synthesis process [2,3]. The recently discovered nanostructured talc (monolayer and few-layered flakes) presents adequate properties to improve the mechanical properties of fragile materials. Such material was firstly obtained in 2015 [4] through mechanical exfoliation of soapstone, and it presents properties similar to those of graphene, such as the in-plane mechanical resistance and the 2D elastic modulus. Few-layered talc sheets are also flexible enough to form folds, however, because talc the monolayer is more than one atom thick its value of flexural rigidity is thirty times larger than that of graphene. Such properties, layer flexibility, and in-plane resistance make nanostructured talc an excellent candidate to be employed as secondary phase material for reinforcement purposes. Besides, talc from soapstone is a low cost and widely available material, which makes it a very viable option. However, to the best of our knowledge, biocompatibility tests on talc from soapstone have not been performed nor talc has been incorporated in HA yet.

Talc from soapstone, which has the chemical formula $Mg_3Si_4(OH)_2$, is composed of biocompatible elements [5,6], which suggests that talc itself may be biocompatible. In the present work, talc was incorporated in HA films in different quantities to improve mechanical properties without reducing HA biocompatibility. The electrodeposition technique was chosen based on its ability to produce different coatings (metals, polymers, ceramics, and composites), its low cost and synthesis ease [7–11]. The electrodeposition process is performed by the action of an electric current that flows between the working electrode (sample) and the counter electrode, both immersed in an electrolyte containing the desired ions be deposited [12]. A second phase, talc, for instance, can be incorporated into the coating during the electrodeposition by suspending it in the electrolyte by agitation and/or use of surfactants. The kinetics of second phase incorporation into the film is usually described by models that may consider the effects of electric, diffusion, and gravity forces. Several models have been proposed to describe the incorporation of secondary phases within a matrix during the electrodeposition process, several of them are detailed in the work of Lelevic and Walsh [13]. The electrodeposited composite films were chemically, morphologically and physically evaluated through scanning electron microscopy, X-ray diffractometry, Raman spectroscopy, polarization curves, and wear tests. Films biocompatibility was evaluated by AlamarBlue®, collagen production, and alkaline phosphatase (ALP).

2. Experiments: material and methods

2.1. Sample pretreatment

Ti samples (Grade 2, see composition in Table 1), 10 mm in diameter and 1 mm thick were mechanically cut from a titanium rod. Samples were wet-ground with SiC emery paper to 1200 grit. After griding samples were ultrasonically cleaned in acetone for 10 min followed by rinsing in methanol and bi-distilled water. To improve the HA coating adherence samples were immersed in 4% hydrofluoric acid for 2 min [14].

Table 1
Chemical composition of titanium samples (Grade 2) as specified by the supplier (TiBrasil).

Element	Composition (wt%)
N	0.01
C	0.01
H	0.0023
Fe	0.07
O	0.14
Ti	Balance

2.2. Hydroxyapatite and composite coating deposition

HA coatings were pulsed electrodeposited from an electrolyte containing 0.042 M $Ca(NO_3)_2{\cdot}4H_2O$, 0.025 M $NH_4H_2PO_4$ and 0.15 M $NaNO_3$, pH = 4.19. Hydrogen peroxide (2%) was added to the electrolyte to reduce hydrogen evolution and improve the adhesive strength between coating and substrate [15]. The electrodeposition process was performed in a three-electrode cell fitted with the titanium sample as the cathode, a graphite bar as the counter-electrode and a saturated calomel electrode (SCE) as the reference electrode. A stirrer was used to keep constant the electrolyte concentration at the cathode surface. The electrolyte temperature (65 °C) was controlled by a thermostatic bath.

Electrodeposition of pristine HA coatings was performed at pulsed potentiostatic mode imposing different cathodic potentials at a frequency of 2 Hz. More compact and uniform films were obtained at −5 V for 1 h. Composite coatings (HA/talc) were deposited with the same electrochemical parameters by adding 10 g/l (T10), 40 g/l (T40) and 80 g/l (T80) of talc flakes to the electrolyte. A stirrer was used during the electrodeposition to keep talk flakes suspended into the electrolyte. The source of talc used in this work, soapstone, was purchased in Ouro Preto (Brazil). As previously reported by Alencar et al. [4], the soapstone talc from Ouro Preto presented exceptional mechanical properties. Talc flakes were obtained from unpolished soapstone by mechanical scraping and sieving.

2.3. Characterization of HA coatings

2.3.1. Scanning electron microscopy characterization

Scanning electron microscopy (SEM) images of HA coatings and energy dispersive spectroscopy (EDS) analysis were performed in a Vega3 Tescan at an acceleration voltage of 20 kV. A carbon coating was used to cover HA samples.

2.3.2. Raman characterization

Raman spectra were recorded in backscattering geometry with a Witec Alpha 300 Instrument employing an excitation wavelength of 532 nm and a grating of 600 grooves mm^{-1}. The laser power was kept at 5 mW while using an objective of 100×.

2.3.3. X-ray diffraction

The crystalline structure of HA coatings was investigated by X-ray diffraction patterns. The X-ray diffraction patterns were obtained using a Bruker D8 Advance Davinci X-ray diffractometer, model D8 Advance, with Cu Kα radiation (λ = 1.5406 Å) with a scan range of 10–80°, a step size of 0.02° and a measuring time of 2 s per point. Diffraction patterns were defined by comparing them with the crystallographic Joint Committee on Powder Diffraction Standards (JCPDS).

2.3.4. Corrosion behavior

The corrosion behavior of the samples was evaluated through potentiodynamic polarization curves in a simulated body fluid environment (phosphate-buffered saline solution (PBS)) at a scan rate of 0.167 mV/s using an Autolab PGSTAT128N potentiostat. The PBS solution used was composed of 8 g/l NaCl; 0.2 g/l KCl; 0.594 g/l Na_2HPO_4 and 0.2 g/l KH_2PO_4, pH = 7.1. The tests were performed in a three-electrode cell. A saturated calomel electrode (SCE) was used as a reference electrode and platinum wire as a counter electrode. The exposed area of the samples (0.253 cm^2) was determined by an o-ring. Before the beginning of the corrosion tests, the system was maintained 1 h in the solution to stabilize the open circuit potential (OCP).

2.3.5. Wear tests

The wear tests were conducted with a ball-on-plate type wear test machine computationally controlled (UMT TRIBOLAB, Bruker). The apparatus operates by rubbing a 6.15 mm diameter alumina ball against

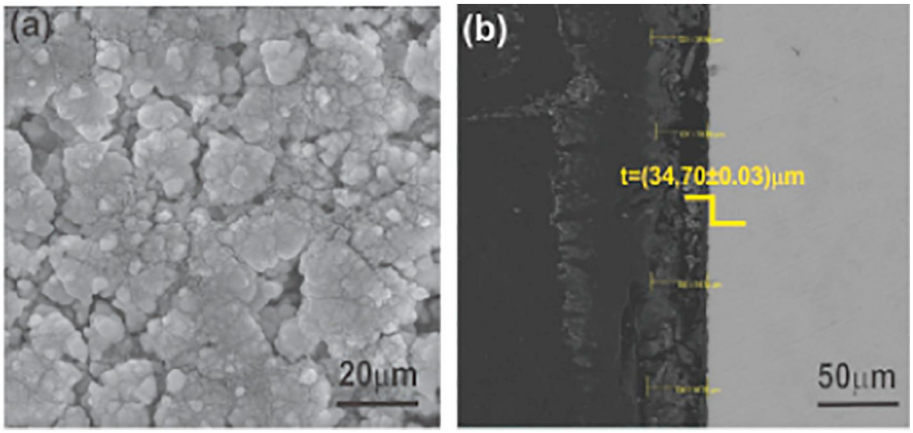

Fig. 1. SEM images of pristine HA coating morphology (a) and thickness (b) pulse electrodeposited at −5 V, 2 Hz during 1 h. SEM magnification 2600 x.

the sample. Reciprocating wear tests were carried out with an applied force of 2 N, the velocity of 2 mm/s and a linear wear track of 2 mm. The wear tracks were measured and examined with an optical microscope.

2.4. In vitro tests

2.4.1. Osteoblast extraction

The biocompatibility of the coatings was tested in vitro with the primary culture of osteoblasts extracted from the calvary of 3 to 5 days-old neonatal Wistar rats [16]. Animals were euthanized by a lethal dose of 2% Lidocaine Hydrochloride without a constrictor vessel. The calvaries of the animals were exposed by performing bilateral clipping and skin retraction, starting from the eye rhyme to the ears. Then, after clipping the suture regions around the parietal bones, they were detached and placed in saline phosphate buffer (PBS) containing penicillin and streptomycin. The samples were fragmented and subjected to enzymatic treatment in 1% trypsin-EDTA for 10 min, followed by four sequential incubations with 2% collagenase baths at 37 °C for 20 min each. The last three baths were centrifuged and the pellets resuspended in supplemented Dulbecco's Modified Eagle's Medium (DMEM) supplemented with 10% fetal bovine serum, penicillin (100 IU/ml) and streptomycin (100 mg/ml). Then the cell suspension was transferred to T25 cell culture bottles containing 5 ml of supplemented DMEM. The cells were led to grow in an incubator at 37 °C in a 5% CO_2 atmosphere. All experiments were conducted in the second cell passage.

2.4.2. Biocompatibility test

After sterilized, the sample was transferred to 24 well, and cell culture plates where they were humidified with PBS overnight in an incubator at 37 °C in a 5% CO_2 atmosphere. Subsequently, PBS was removed and 1×10^5 osteoblasts were plated onto each sample with supplemented DMEM culture medium. The culture medium was renewed every 2–3 days, and on days 3, 7 and 14, 10% (v/v) of AlamarBlue™ Cell Viability Reagent (Invitrogen) was added to the wells and the plates were kept in an incubator under cell culture conditions. After incubation for 4 h a fluorescence at 530 nm excitation and 590 nm emission wavelengths were performed (Varioskan™ LUX multimode microplate reader).

2.4.3. Collagen production

Supernatant from each well was collected on days 3, 7 and 14 for analysis of collagen production. Analyzes were performed by colorimetric kit using the Sircol™ Soluble Collagen Assay (Biocolor), according to the manufacturer's instructions.

2.4.4. Alkaline phosphatase (ALP) activity

ALP activity was evaluated using the BCIP-NBT assay. The supernatants from each well were removed on days 7 and 14, the wells were washed with PBS and then 200 μl of BCIP-NBT solution, which was prepared according to the manufacturer's recommended protocol, was added to each well. After 2 h of incubation at 37 °C in a 5% CO_2 atmosphere, the solution was replaced with 200 μl of SDS containing 10% of HCl and the plates were incubated overnight at 37 °C to promote cell lysis and an optical density measurement at 595 nm was performed (Varioskan™ LUX multimode microplate reader) [17].

2.4.5. Scanning electron microscopy (SEM) characterization

The morphology of osteoblasts adhered to the samples was determined using SEM after 14 days of culture. Cells were fixed in a solution containing paraformaldehyde 4% and Glutaraldehyde 0.5% for 10 min at 4 °C. After fixation, the PBS was replaced by a 1% osmium tetroxide (OsO4) solution in PBS pH 7.4. Then, cells were dehydrated in increasing concentration of ethanol (35%, 50%, 70%, and 100%) for 10 min each. The surfaces were coated with 10 nm of gold and stored in a desiccator until analysis using SEM (TM3000) imaging.

3. Results and discussion

3.1. SEM and EDS

3.1.1. Pristine HA coatings

Fig. 1(a) and (b) shows the morphology and thickness of pristine HA coating pulsed deposited at the best conditions tested: -5 V, 2 Hz, for 1 h. SEM images show that coatings are composed of rough and well compact grains with no identified defects. The deposition of well compact deposits with low amounts of defects can be ascribed to the pulsed deposition technique and to the addition of hydrogen peroxide. In comparison to the conventional potentiostatic deposition, the pulsed electrodeposition reduces the adverse effects of concentration polarization and allows the hydrogen bubbles, produced in the process, to escape at pulse off [18,19]. The addition of hydrogen peroxide induces the production of OH^- ions on the cathode diminishing the effects of the H_2 [15]. Fig. 1(b) also shows a mean coating thickness, of about 34.70 μm, obtained during 1 h of deposition.

3.1.2. Talc from soapstone

With the aim to improve the mechanical properties of the ceramic coatings, a second phase, talc from soapstone, was added to the electrolyte to be incorporated into them. SEM image of talc platelets and size distribution is shown in Fig. 2. It can be seen that talc platelets are composed of a layered structure with lateral dimensions varying roughly between 29 μm and 120 μm. Talc thickness were not measured

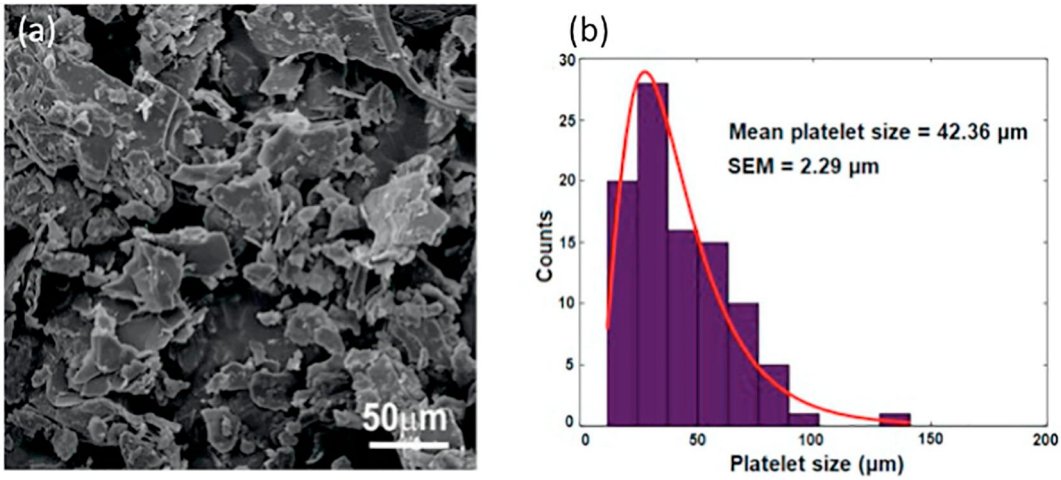

Fig. 2. (a) SEM image of talc platelets obtained from an unpolished soapstone after mechanical scraping. SEM magnification 1000 x. (b) Size distribution of talc platelets.

but it is possible to observe from SEM images that the aspect ratio, lateral dimensions/thickness are high. The size distribution was acquired from a lower SEM magnification (400 X) to have a representative sample of talc platelets. The average platelet size is about 42.36 μm.

3.1.3. Composite HA/talc coatings

Fig. 3 shows a composite coating electrodeposited in an electrolyte containing 10 g/l of talc (T10). The figure shows that the addition of talc does not modify the basic morphology of the coating, which is still composed of rough and compact grains. The incorporation of talc leads to a more compact structure probably because the matrix interconnection effect, which results from the presence of a material whose lateral dimensions are much larger than its thickness. Pei et al. [14] have shown that the incorporation of secondary phase with high aspect ratio, such as carbon nanotubes, binds the coating structure together. Also, Janković et al. [3] have shown that graphene effectively acts as a nano reinforcement filler and prevents the creation and propagation of cracks. Fig. 3 also shows a talc platelet (see dark circle), which is an evidence of the incorporation of talc into the HA coating.

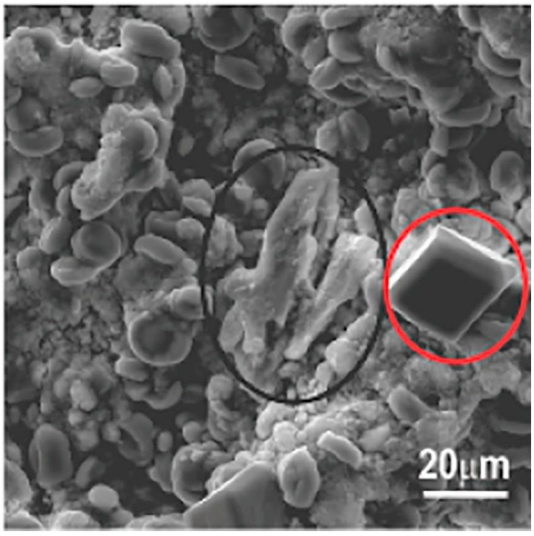

Fig. 3. HA coating electrodeposited in an electrolyte containing 10 g/l of talc (T10). The coating was pulse deposited at −5 V, 2 Hz, during 1 h. The dark circle shows a talc platelet and the red circle shows crystals of calcium phase. SEM magnification 2600 x. (For interpretation of the references to colour in this figure legend, the reader is referred to the web version of this article.)

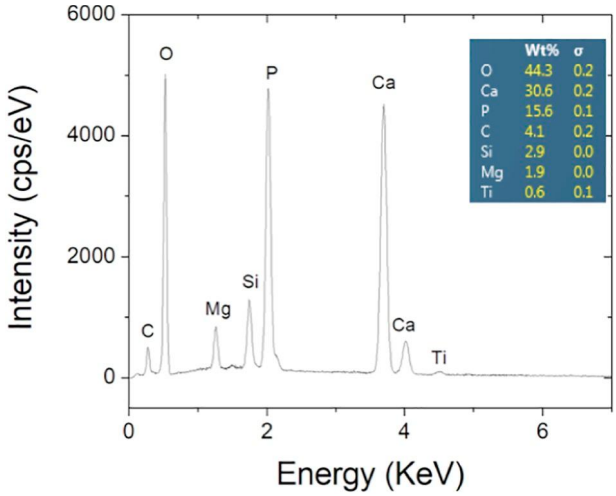

Fig. 4. EDS spectra of HA coating with the addition of 10 g/l of talc (T10) in the electrolyte. The coating was pulse deposited at −5 V, 2 Hz, for 1 h.

Fig. 4 shows the EDS spectra revealing the presence of Mg and Si, the main components of talc. The EDS also shows that the electrodeposited HA coatings present a Ca/P ratio of 1.96. Ratios above the stoichiometric values, 1.67 for pure HA, may indicate the presence of CaO or $Ca(OH)_2$ [16,17,20]. The coating contains a small amount of well-faceted crystals (see circles in Fig. 3). EDS analysis reveals that such crystals have high Ca concentration suggesting the formation of phases like CaO, $Ca(OH)_2$ or $CaCO_3$ [9,10].

3.2. Raman spectroscopy

For completeness of SEM characterization, we have also employed Raman spectroscopy characterization of pristine HA coatings to determine the morphology and composition of the coatings and crystals. Fig. 5 presents the characterization results obtained employing Raman spectroscopy for the same coatings discussed earlier. To investigate the homogeneity of HA coatings, we took spectra at different locations for all films. Fig. 5(a), (b) and (c) give the images, taken using the spectrometer-coupled optical microscope, of the investigated areas, whereas Fig. 5(d) and (e), the acquired Raman spectra at two distinct points within the sample. Spectra in Fig. 5(d) and (e) are representative Raman spectra of these coatings. From the images, the sample appears

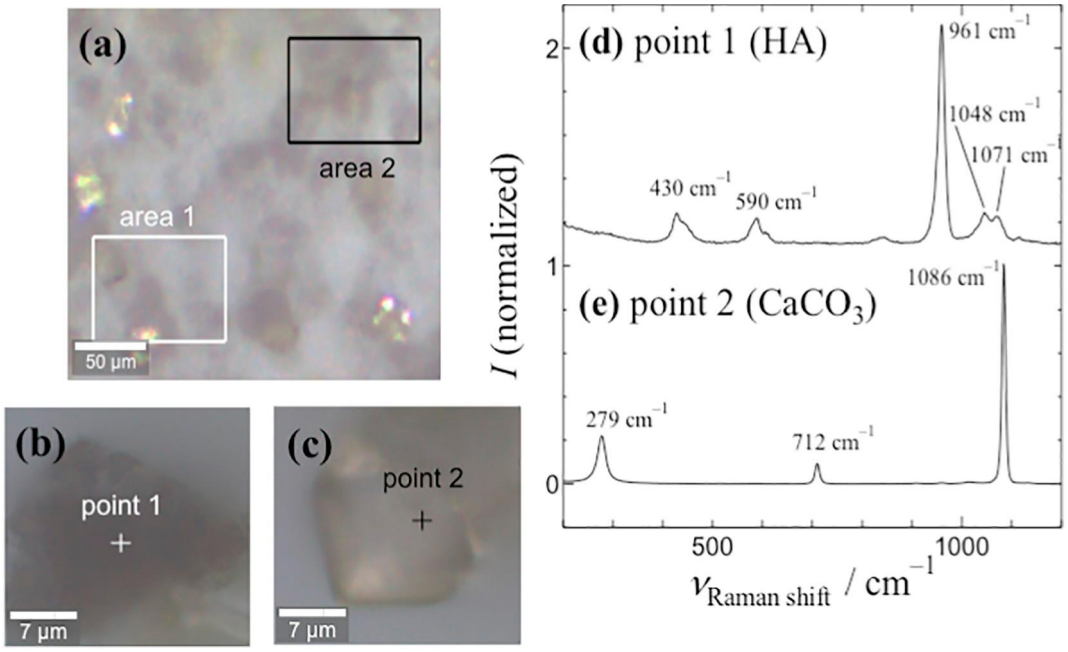

Fig. 5. Raman spectroscopic analysis of HA coatings. (a), (b) and (c) images of the investigated areas. A representative spectrum of (d) pristine HA coatings and (e) $CaCO_3$ present in the coating.

heterogeneous in texture, presenting similar morphology as the SEM images did. Two regions can be distinguished in the coatings: one containing dark coarse structures (Fig. 5(b)) and another one bearing a little amount of light-colored crystals (Fig. 5(c)). The Raman spectra of these two regions were observed to be completely different: the latter being characterized by three pronounced peaks at 279 cm^{-1}, 712 cm^{-1}, and 1086 cm^{-1}, while the former by bands with maxima at 430 cm^{-1}, 590 cm^{-1}, 961 cm^{-1}, 1048 cm^{-1} and 1071 cm^{-1}. The first four Raman bands of this last group can be attributed to the ν_2, ν_4, ν_1, and ν_3 vibrational modes, respectively, expected for the phosphate ion in HA coatings [22–24]. The fifth mode at 1071 cm^{-1} has been assigned to a combination of a carbonate mode with a phosphate one [25]. Indeed, the three distinct peaks of the spectrum from point 2 (Fig. 5(e)) indicate the presence of little amounts of $CaCO_3$ [26] crystals also observed in SEM images.

3.3. X-ray diffraction

We have also employed X-ray diffraction to corroborate the Raman results and access the crystalline structure of the talc and HA coatings.

3.3.1. Pristine HA coatings

Fig. 6 shows the X-ray spectrum obtained for pristine HA coating. The titanium substrate gives rise to the most intense peaks observed in the spectrum. Peaks related to calcium phosphate hydroxide ($Ca_5(PO_4)_3(OH)$) phase (JCPDS 09-0432) confirms the deposition of HA coatings through pulsed electrodeposition. In agreement to Raman results, a calcium carbonate phase (JCPDS 96-210-3120) is observed. Molecules and ion of the environment may lead to the formation of carbonate phases according to the following reactions:

$$Ca^{+2} + 2OH^{-} = Ca(OH)_2 \quad (1)$$

$$CO_2 + H_2O = H_2CO_3 \quad (2)$$

$$H_2CO_3 + Ca(OH)_2 = CaCO_3 + 2H_2O \quad (3)$$

According to the above equations, $Ca(OH)_2$ is formed from ions of electrolyte solution during the electrodeposition process (Eq. (1)). Later, the coating is exposed to moist air, allowing H_2CO_3 molecules (see Eq. (2)) to react with $Ca(OH)_2$ resulting in the $CaCO_3$ carbonate

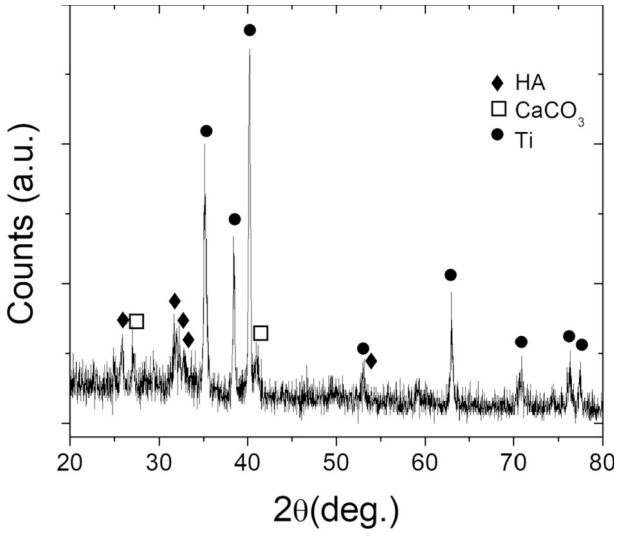

Fig. 6. X-ray spectrum of pristine HA coating pulsed electrodeposited on titanium substrate.

phase (Eq. (3)). The formation of calcium hydroxide during the electrodeposition is consistent with previous results of Ansari et al. [21], who have observed the calcium hydroxide formation in addition to HA obtained by aqueous precipitation reaction.

The calcium carbonate phase present in the coatings should not be a problem for biomedical applications because it is easily converted to carbonated hydroxyapatite when in a PBS solution. Tang et al. [27] have shown that calcium carbonate particles begin to dissolve just after being soaked in PBS solution. The released Ca^{+2} ions react with PO_4^{-3}, HPO_4^{-2}, and OH^{-} ions in PBS to form carbonate hydroxyapatite. The general reaction can be expressed as follows:

$$(10 - x - y/2)Ca^{+2} + xHPO_4^{-2} + (6 - x - y)PO_4^{-3} + yCO_3^{-2} + (2 - x)OH^{-} = Ca_{10-x-y/2}(HPO_4)_x(PO_4)_{6-x-y}(CO_3)_y(OH)_{2-x} \quad (4)$$

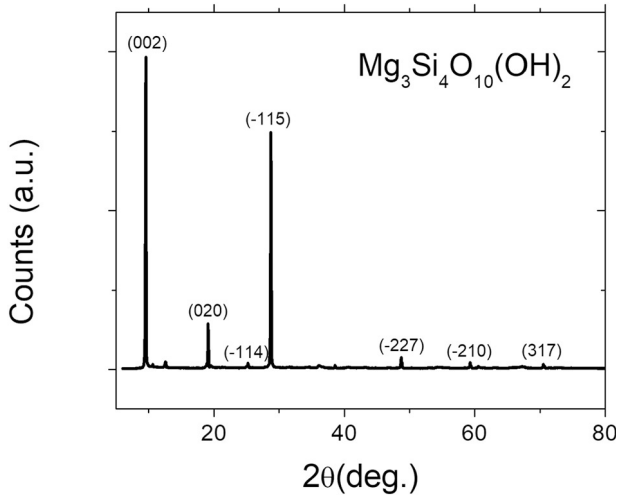

Fig. 7. X-ray spectrum of talc platelets from unpolished soapstone.

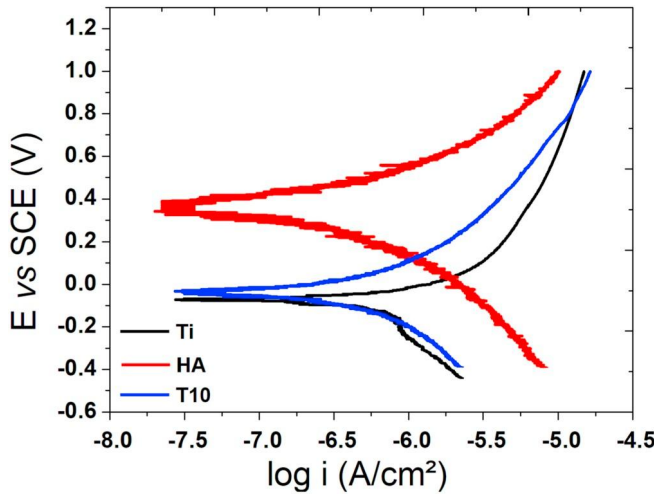

Fig. 8. Potentiodynamic polarization curves in PBS solution for bare titanium (Ti), pristine HA coating (HA) and HA with the incorporation of 10 g/l of talc in the electrolyte (T10). Sweep rate: 0.167 mV/s.

Table 2
Corrosion current densities obtained from Tafel plot for different tested samples.

Sample	i_{corr} (A/cm^2)
Bare titanium (Ti)	1.6×10^{-7}
Pristine HA coating (HA)	7.9×10^{-8}
HA/talc coating (T10)	1.3×10^{-7}

3.3.2. *Talc from soapstone*

Fig. 7 shows the X-ray structural characterization of our talc platelets. Such an X-ray spectrum is characteristic of Monoclinic Talc ($Mg_3Si_4O_{10}(OH)_2$) indexed from the JCPDS database (02–0569).

3.4. *Corrosion behavior*

We employed potentiodynamic polarization curves to evaluate the corrosion behavior of HA coatings with and without incorporation of talc in PBS solution (to simulate the body environment). The results in Fig. 8 are for bare titanium, HA coating and HA coatings with talc incorporation (T10). From the presented curves, we have extrapolated Tafel lines and estimated corrosion current density of the samples, see Table 2. The titanium polarization curve shows a corrosion potential

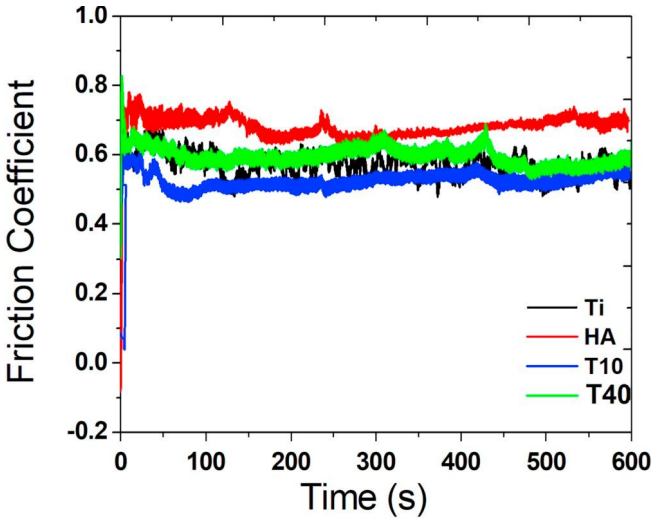

Fig. 9. Friction coefficient of bare Ti, pristine HA, composites T10 and T40 developed during wear test. Wear tests were performed at a normal load of 2 N, velocity of 2 mm/s and a linear wear track of 2 mm.

Table 3
Wear track length for different coatings and materials tested on a ball-on-plate tribometer at 2 N, 2 mm/s and a wear track of 2 mm.

Sample	Wear track length (μm)
Ti	1001
HA	439
T10	303
T40	437
T80	536

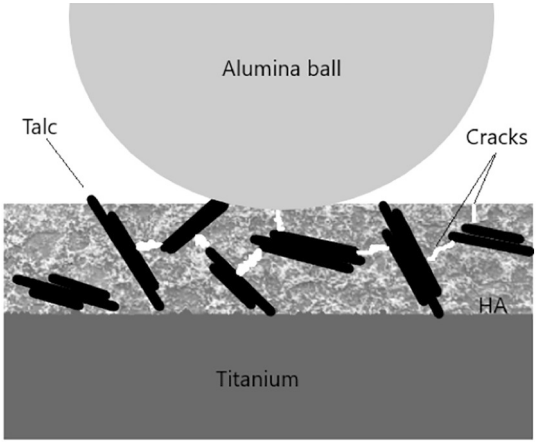

Fig. 10. Schematic drawing showing the occurrence of the cracks due to platelets excess. The matrix cross section is reduced by talc platelets excess and does not support the rubbing load.

around −70 mV [28,29] and leads to a corrosion current density of about 10^{-7} A/cm^2. The corrosion current density decreases to half of this value when the titanium substrate is protected with HA coatings, which shows an important increase in corrosion resistance. Ceramic HA coatings without or with low amounts of defects are expected to provide protection to the substrate since they provides physical barriers, between the metal substrate and the electrolyte, which are not degraded by the environment [30].

Besides, the HA-coated titanium is also nobler than the bare substrate, with higher corrosion potential (around 350 mV) and lower

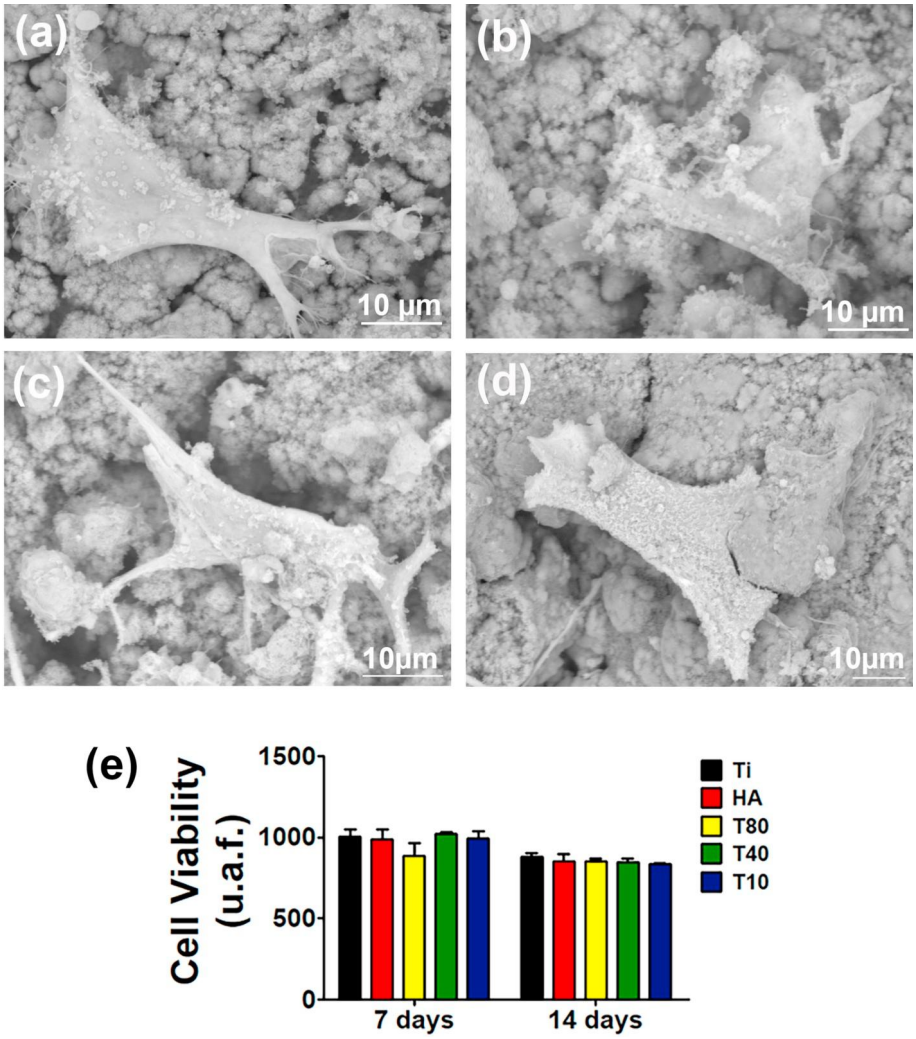

Fig. 11. (a)–(d) SEM images of osteoblast cells seeded on different surface coatings over a period of 14 days: (a) HA, (b) T80, (c) T40 and (d) T10. (e) Osteoblast cell viability cultured on Ti, HA, T80, T40, T10. Cell viability was assessed by Alamar Blue® after 7 and 14 days of cell culture. The data are expressed as the mean ± SEM. *** $p < 0.001$ as measured using two-way ANOVA, $n = 3$.

anodic current densities (up to 1 V) than the respective values for bare titanium. This increase in corrosion behavior indicates the formation of compact coatings, as observed by SEM. The corrosion behavior of HA coatings with talc incorporation (T10) is similar to that of bare titanium (see also Table 2), suggesting the presence of cracks or voids in the coating [2]. Also, the talc flakes, whose dimensions are larger than the coating thickness, may create an interface that connects the Ti substrate to the solution, serving as a passageway for the electrolyte to reach the substrate. HA coatings with the addition of 40 g/l (T40) and 80 g/l (T80) of talc to the electrolyte present the same corrosion profile presented by T10 coatings (not shown in Fig. 8).

3.5. Wear tests

We employed the ball on plate wear tests to evaluate the mechanical properties of coatings. It is important to point out that material intrinsic surface properties such as strength, hardness, ductility, etc. are very important factors for its wear resistance. However, other factors like surface finish, lubrication, load, speed, properties of the opposing surface, etc. are equally important. In this sense, the response of wear tests (friction coefficient, depth, and width of wear track, the morphology of wear track) is a combination of several mechanical properties.

Fig. 9 shows the friction coefficient obtained from the wear tests on bare titanium, pristine HA, composites HA/talc (T10 and T40). Bare titanium samples present a mean friction coefficient of about 0.58, while it is about 0.68 for HA coating. Despite the higher fiction coefficient of HA coating, the wear track width is much lower than that observed for bare titanium (an observed decrease of about 56% in the wear track width, see Table 3), which indicates an increase in wear resistance conferred by the HA coating. The augmented friction coefficient of the HA coating can be related to differences in the surface finishing of materials, or it can be an intrinsic characteristic of HA coatings; meanwhile, the lower wear width is related to the HA hardness, which is higher than that of Ti. Buciumeanu et al. [31] observed an increase in the friction coefficient of Ti6Al4V by making a composite of Ti6Al4V and HA. The authors attribute the increase in friction coefficient to the presence of the HA phase (harder than Ti6AL4V alloy), which increases the hardness of the composites.

By adding 10 g/l of talc to HA coatings (T10), we observe a decrease in friction coefficient ($\mu = 0.52$). In agreement with the decrease in friction coefficient, the wear track width also decreases to about 300 μm. The friction coefficient and the wear track reduction are ascribed to the lubricating action of talc platelets. The talc itself is a lubricating material characterized by van der Walls bonds between layers [4]. Interestingly, the addition of a higher amount of talc (40 g/l and 80 g/l) increases the friction coefficient and the wear track width. This occurrence may be ascribed to the matrix disintegration that is due to the excess of platelets and loading action (see schematic drawing in

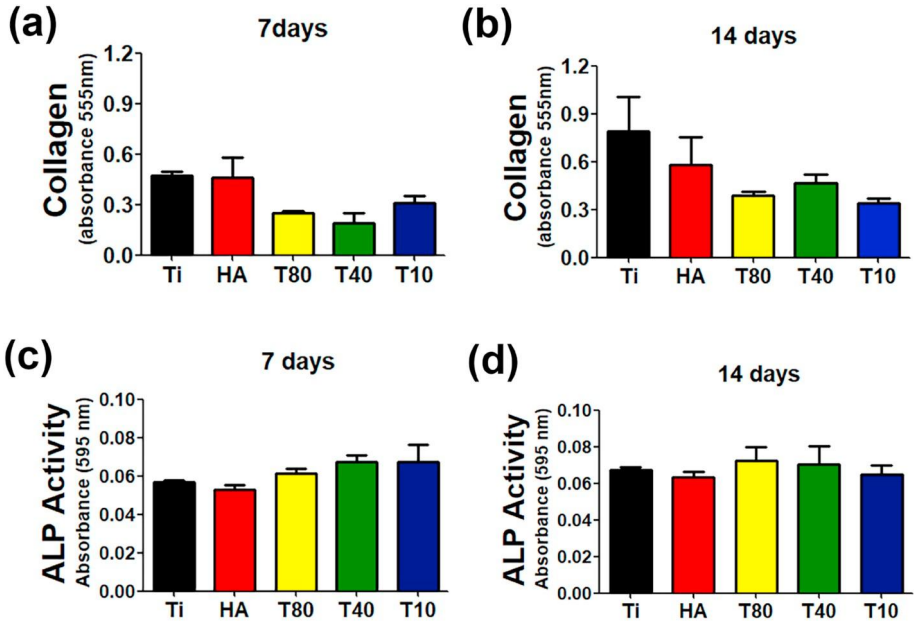

Fig. 12. Collagen production after 7 (a) and 14 (b) days of culture. Alkaline phosphatase activity after 7 (c) and 14 (d) days of culture. Data are expressed as the mean ± SEM. Measured using ANOVA, n = 3.

Fig. 10). During the rubbing, the excess of platelet reduces the matrix cross-section that does not support the rubbing load and cracks itself, leaving third body particles.

In agreement to the present study, other works also shows that addition of secondary phases improves wear resistance of pristine HA [32–35]. Lahiri et al. [32] have shown that the addition of 4 wt% carbon nanotubes to HA coating reduces the volume of wear debris generation by 80% as a result of the improvement in elastic modulus and fracture toughness. Mittal et al. [34] added Al_2O_3 secondary phase to HA coatings and observed an increase of wear resistance with the Al_2O_3 content. In this case, authors ascribe the mechanical improvement to the lubricating effect and hardness of Al_2O_3 secondary phase.

3.6. Biocompatibility tests

3.6.1. Viability

The sample's biocompatibility is a fundamental parameter for the biological study and the use of implants. In this sense, the cytocompatibility was characterized by seeding osteoblast cells on the different samples studied in this work. Scanning electron microscopy was employed to access osteoblast cell morphology and attest cell adhesion on different coatings (HA, T10, T40, and T80), see Fig. 11(a–d). The biocompatibility of the different samples studied in this work was measured by evaluating the viability of the cells and proliferation through the Alamar Blue® test, see Fig. 11(e).

SEM images show that osteoblast cells adhere to the different coating surfaces they are grown on, besides they present typical osteoblast morphology with cytoplasmatic extensions indicating that the tested coatings are biocompatible with bone cell tissue [2]. Osteoblast cell viability analysis reveals that coatings with the highest talc concentration have under viability in 7 days of culture compared to the other samples. The lower viability presented by the composite coating with highest talc amount (T80) may be due to talc hydrophobic character [36]. On the other hand, this trend was reversed on 14th culture day, showing good osteocompatibility and absence of citotoxicity. Thus, because of its hydrophobic character, talc reduces viability at the first days of culture, but because talc is not cytotoxic, cells are able to recover themselves at 14 days.

3.6.2. ALP activity and collagen production

Alkaline phosphatase is one of the first functional genes expressed in the calcification process [37,38]. ALP is widely used as an osteoblast marker, and the increased ALP activity is associated with the calcification process and osteoblastic differentiation. From the ALP results (see Fig. 12(c) and (d)) one can conclude the bone maturation improves in as much as the talc concentration in the coatings increases. The observed improvement in bone maturation with increasing talc content may be ascribed to the presence of magnesium. Magnesium, one of the main components of talc, is an important agent of bone maturation and it is known to improve ALP activity [39,40].

On the other hand, our data (see Fig. 12(a) and (b)) show higher collagen production for bare Ti and pristine HA compared to composite coatings. When cells enter the differentiation period, the proliferation rate decreases and consequently the collagen expression decreases and ALP begins to be actively expressed [41]. From these results, our data suggest that our biocomposites (HA/talc) favor the differentiation process of osteoblasts.

In summary, the presented results demonstrate the good biocompatibility of composite coatings, which indicates that talc is biocompatible and favors bone maturation.

4. Conclusion

We successfully employed pulsed electrodeposition to produce HA and HA/talc coatings. Pristine and composite coatings (HA/talc), both composed of well-compacted grains, improve the corrosion resistance of titanium substrates. Wear tests indicate that HA/talc composites present much better mechanical properties than pristine HA coatings and bare Ti, i. e., lower wear track and lower friction coefficient. Biocompatibility tests confirm that composite coatings are biocompatible and induce cellular proliferation and bone maturation. In summary, our results show that it is possible to use a simple technique and cheap and widely available materials to obtain improved composite coatings with potential for biomedical applications, in particular, in dental and orthopedic implants.

CRediT authorship contribution statement

Laureana Moreira Mota:Investigation.**Daniel Nilson Nunes Nicomedes**:Investigation.**Ana Paula Moreira Barboza**:Investigation, Methodology.**Sérgio Luís Lima de Moraes Ramos**:Investigation. **Rebecca Vasconcellos**:Investigation.**Nathanael Vieira Medrado**:Investigation.**Érika Costa de Alvarenga**:Supervision. **Giovanna Machado**:Resources.**Karyne R.C. Juste**:Resources. **Cláudia Karina de Vasconcelos**:Resources.**Ariete Righi**:Resources.**Sara Matte Manhabosco**:Investigation.**Rodrigo Ribeiro Resende**:Resources.**Ronaldo Junio Campos Batista**:Writing - review & editing.**Jaqueline dos Santos Soares**:Writing - review & editing, Funding acquisition.**Taíse Matte Manhabosco**:Funding acquisition, Supervision, Writing - review & editing.

Declaration of competing interest

The authors certify that they have NO affiliations with or involvement in any organization or entity with any financial interest (such as honoraria; educational grants; participation in speakers' bureaus; membership, employment, consultancies, stock ownership, or other equity interest; and expert testimony or patent-licensing arrangements), or non-financial interest (such as personal or professional relationships, affiliations, knowledge or beliefs) in the subject matter or materials discussed in this manuscript.

Acknowledgments

We would like to thank M. A. Pimenta for laboratory space for Raman measurements in the Laboratory of Raman Spectroscopy/UFMG. Also, we thank A. Freitas for the particle size analysis. Authors acknowledge the financial support from Federal University of Ouro Preto/PROPP (Brazil, grant number 23109.004080/2019-88), Conselho Nacional de Desenvolvimento Científico e Tecnológico (Brazil, grant number 421558/2018-0), CAPES (Brazil), FAPEMIG (Brazil, grant number PPM-00455-18), FAPERGS (grant number 19/2551-0001349-3) and L'Oréal/UNESCO/ABC (Brazil). We also thank the NanoLab Laboratory from the Federal University of Ouro Preto for the SEM images.

References

[1] L.L. Hench, R.J. Splinter, W.C. Allen, T.K. Greenlee, Bonding mechanisms at the interface of ceramic prosthetic materials, J. Biomed. Mater. Res. 2 (1971) 117–141, https://doi.org/10.1002/jbm.820050611.

[2] Y. Zeng, X. Pei, S. Yang, H. Qin, H. Cai, S. Hu, L. Sui, Q. Wan, J. Wang, Graphene oxide/hydroxyapatite composite coatings faricated by electrochemical deposition, Surf. Coat. Technol. 286 (2016) 72–79, https://doi.org/10.1016/j.surfcoat.2015.12.013.

[3] Ana Jankovic, Sanja Erakovic, Miodrag Mitric, Ivana Z. Matic, Zorica D. Juranic, Gary C.P. Tsui, Chak-yin Tang, Vesna Mišković-Stankovic, Kyong Yop Rhee, Soo Jin Park, Bioactive hydroxyapatite/graphene composite coating and its corrosion stability in simulated body fluid, J. Alloys Compd. 624 (2015) 148–157, https://doi.org/10.1016/j.biomaterials.2005.10.003.

[4] A.B. Alencar, A.P.M. Barboza, B.S. Archanjo, H. Chacham, B.R.A. Neves, Experimental and theorical investigations of monolayer and few-layer talc, 2D Mater. 2 (2015) 015004, , https://doi.org/10.1088/2053-1583/2/1/015004.

[5] J.R. Henstock, L.T. Canham, S.I. Anderson, Silicon: the evolution of its use in biomaterials, Acta Biomater. 11 (2015) 17–26, https://doi.org/10.1016/j.actbio.2014.09.025.

[6] M.P. Staiger, A.M. Pietak, J. Huadmai, G. Dias, Magnesium and its alloys as orthopedic biomaterials: a review, Biomaterials 27 (2006) 1728–1734, https://doi.org/10.1016/j.biomaterials.2005.10.003.

[7] V.F.L. Filho, G. Machado, R.J.C. Batista, J.S. Soares, A.B. de Oliveira, C. de Vasconcelos, A.L. Lino, T.M. Manhabosco, Effect of TiO_2 nanoparticles on polyaniline films electropolymerized at different pH, J. Phys. Chem. C 120 (2016) 14977–14983, https://doi.org/10.1021/acs.jpcc.6b04919.

[8] T.M. Manhabosco, L.A.M. Martins, S.M. Tamborim, M. Ilha, M.Q. Vieira, F.C.R. Guma, I.L. Müller, Cell response and corrosion behavior of electrodeposited diamond-like carbon films on nanostructured titanium, Corros. Sci. 66 (2013) 169–176, https://doi.org/10.1016/j.corsci.2012.09.015.

[9] T.M. Manhabosco, I.L. Müller, Deposition of thin cobalt films onto silicon by galvanostatic and potentiostatic techniques, J. Mater. Sci. 44 (2009) 2931–2937, https://doi.org/10.1007/s10853-009-3388-9.

[10] T.M. Manhabosco, G. Englert, I.L. Müller, Characterization of cobalt thin films electrodeposited onto silicon with two different resistivities, Surf. Coat. Technol. 200 (2006) 5203–5209, https://doi.org/10.1016/j.surfcoat.2005.06.005.

[11] T.M. Manhabosco, S. Aloni, T.R. Kuyendall, S.M. Manhabosco, A.B. Batista, J.S. Soares, A.P.M. Barboza, A.B. Oliveira, R.C. Batista, J.J. Urban, Electrochemical atomic layer epitaxy deposition of ultrathin SnTe films, Recent Prog. Mater. 1 (2019) 12, https://doi.org/10.21926/rpm.1904005.

[12] A.A. Pasa, M.L. Mundford, Encyclopedia of Chemical Processing, v. 1, Taylor & Francis, 2006, pp. 821–832, https://doi.org/10.1081/E-ECHP-120037171.

[13] A. Lelevica, F.C. Walsh, Electrodeposition of Ni-P composite coatings: a review, Surf. Coat. Technol. 369 (2019) 198–220, https://doi.org/10.1016/j.surfcoat.2019.03.055.

[14] X. Pei, et al., Single-walled carbon nanotubes/hydroxyapatite coatings on titanium obtained by electrochemical deposition, Appl. Surf. Sci. 295 (2014) 71–80, https://doi.org/10.1016/j.apsusc.2014.01.009.

[15] X.Y. Chen, Z.W. Zhao, A.L. Chen, H.G. Li, Pulsed electrodeposition of hydroxyapatite on titanium substrate in solution containing hydrogen peroxide, Trans. Nonferrous Metals Soc. China 17 (2007) 617–621, https://doi.org/10.1016/S1003-6326(07)60144-7.

[16] E.C. Alvarenga, R. Rodrigues, A. Caricati-Neto, F.C. Silva-Filho, E.J. Paredes-Gamero, A.T. Ferreira, Low-intensity pulsed ultrasound-dependent osteoblast proliferation occurs by via activation of the P2Y receptor: role of the P2Y1 receptor, Bone 46 (2010) 355–362, https://doi.org/10.1016/j.bone.2009.09.017.

[17] R. Rodrigues-Ribeiro, E.C. Alvarenga, M.L. Calio, E.J. Paredes-Gamero, A.T. Ferreira, Dual role of P2 receptors during osteoblast differentiation, Cell Biochem. Biophys. 71 (2015) 1225–1233, https://doi.org/10.1007/s12013-014-0332-7.

[18] E.C. Meng, S.K. Guan, H.X. Wang, L.G. Wang, S.J. Zhu, J.H. Hu, C.X. Ren, J.H. Gao, Y.S. Feng, Effect of electrodeposition modes on surface characteristics and corrosion properties of fluorine-doped hydroxyapatite coatings on Mg–Zn–Ca alloy, Appl. Surf. Sci. 257 (2011) 4811–4816, https://doi.org/10.1016/j.apsusc.2010.12.073.

[19] D.J. Blackwood, K.H.W. Seah, Galvanostatic pulse deposition of hydroxyapatite for adhesion to titanium for biomedical purposes, Mater. Sci. Eng. C 30 (2010) 561–565, https://doi.org/10.1016/j.msec.2010.02.007.

[20] H. Liu, H. Yazici, C. Ergun, T.J. Webster, H. Bermek, An in vitro evaluation of the Ca/P ratio for the cytocompatibility of nano-to-micron particulate calcium phosphated for bone regeneration, Acta Biomater. 4 (2008) 1472–1479, https://doi.org/10.1016/j.actbio.2008.02.025.

[21] M. Ansari, S.M. Naghib, F. Moztarzadeh, A. Salati, Synthesis and characterization of hydroxyapatite-calcium hydroxide for dental composites, Ceramics-Silikáty 55 (2011) 123–126.

[22] H. Tsuda, J. Arends, Orientational micro-Raman spectroscopy on hydroxyapatite single crystals and human enamel crystallites, J. Dent. Res. 73 (1994) 1703–1710, https://doi.org/10.1177/00220345940730110501.

[23] P.N. de Aza, F. Guitián, C. Santos, S. de Aza, R. Cuscó, L. Artús, Vibrational properties of calcium phosphate compounds. 2. Comparison between hydroxyapatite and β-tricalcium phosphate, Chem. Mater. 9 (1997) 916–922, https://doi.org/10.1021/cm9604266.

[24] S. Koutsopoulos, Synthesis and characterization of hydroxyapatite crystals: a review study on the analytical methods, J. Biomed. Mater. Res. 62 (2002) 600–612, https://doi.org/10.1002/jbm.10280.

[25] A. Awonusi, M.D. Morris, M.M.J. Tecklenburg, Carbonate assignment and calibration in the Raman spectrum of apatite, Calcif. Tissue Int. 81 (2007) 46–52, https://doi.org/10.1007/s00223-007-9034-0.

[26] T. Schmid, P. Dariz, Shedding light onto the spectra of lime: Raman and luminescence bands of CaO, $Ca(OH)_2$ and $CaCO_3$, J. Raman Spectrosc. 46 (2014) 141–146, https://doi.org/10.1002/jrs.4622.

[27] Sha Tang, Bo Tian, Ya-Jun Guo, Zhen-An Zhu, Ya-Ping Guo, Chitosan/carbonated hydroxyapatite composite coatings: fabrication, structure and biocompatibility, Surf. Coat. Technol. 251 (2014) 210–216, https://doi.org/10.1016/j.surfcoat.2014.04.028.

[28] T.M. Manhabosco, I.L. Muller, Electrodeposition of diamond-like carbon (DLC) films on Ti, Appl. Surf. Sci. 255 (2009) 4082–4086, https://doi.org/10.1016/j.apsusc.2012.08.052.

[29] S. Tamilselvi, V. Raman, N. Rajendran, Corrosion behaviour of Ti–6Al–7Nb and Ti–6Al–4V ELI alloys in the simulated body fluid solution by electrochemical impedance spectroscopy, Electrochim. Acta 52 (2006) 839–846, https://doi.org/10.1016/j.electacta.2006.06.018.

[30] E. Yılmaz, B. Çakıroğlu, A. Gökçe, F. Findik, H.O. Gulsoy, N. Gulsoy, Ö. Mutlu, M. Özacar, Novel hydroxyapatite/graphene oxide/collagen bioactive composite coating on Ti16Nb alloys by electrodeposition, Mater. Sci. Eng. C 101 (2019) 292–305, https://doi.org/10.1016/j.msec.2019.03.078.

[31] M. Buciumeanu, A. Araujo, O. Carvalho, G. Miranda, J.C.M. Souza, F.S. Silva, B. Henriques, Study of the tribocorrosion behaviour of Ti6Al4V-HA biocomposites, Tribol. Int. 107 (2017) 77–84, https://doi.org/10.1016/j.triboint.2016.11.029.

[32] D. Lahiri, A.P. Benaduce, F. Rouzaud, J. Solomon, A.K. Keshri, L. Kos, A. Agarwal, Wear behavior and in vitro cytotoxicity of wear debris generated from hydroxyapatite–carbon nanotube composite coating, J. Biomed. Mater. Res. A 96 (2010) 1–12, https://doi.org/10.1002/jbm.a.32952.

[33] D. Lahiri, V. Singh, A.K. Keshri, S. Seal, A. Agarwal, Carbon nanotube toughened hydroxyapatite by spark plasma sintering: microstructural evolution and multiscale tribological properties, Carbon 48 (2010) 3103–3120, https://doi.org/10.1016/j.carbon.2010.04.047.

[34] M. Mittal, S.K. Nath, S. Prakash, Improvement in mechanical properties of plasma sprayed hydroxyapatite coatings by Al2O3 reinforcement, Mater. Sci. Eng. C 33 (2013) 2838–2845, https://doi.org/10.1016/j.msec.2013.03.005.
[35] K. Balani, Y. Chen, S.P. Harimkar, N.B. Dahotre, A. Agarwal, Tribological behavior of plasma-sprayed carbon nanotube-reinforced hydroxyapatite coating in physiological solution, Acta Biomater. 3 (2007) 944–951, https://doi.org/10.1016/j.actbio.2007.06.001.
[36] B. Rotenberg, A. Patel, D. Chandler, Molecular explanation for why talc surfaces can be both hydrophilic and hydrophobic, J. Am. Chem. Soc. 133 (2011) 20521–20527, https://doi.org/10.1021/ja208687a.
[37] A. Yamaguchi, T. Komori, T. Suda, Regulation of osteoblast differentiation mediated by bone morphogenetic proteins, hedgehogs, and Cbfa1, Endocr. Rev. 21 (2000) 393–411, https://doi.org/10.1210/edrv.21.4.0403.
[38] E.E. Golub, G. Harrison, A.G. Taylor, S. Camper, I.M. Shapiro, The role of alkaline phosphatase in cartilage mineralization, Bone Miner. 17 (1992) 272–278, https://doi.org/10.1016/0169-6009(92)90750-8.
[39] L. Wu, F. Feyerabend, A.F. Schilling, R. Willumeit-Römer, B.J.C. Luthringer, Effects of extracellular magnesium extract on the proliferation and differentiation of human osteoblasts and osteoclasts in coculture, Acta Biomater. 27 (2015) 294–304, https://doi.org/10.1016/j.actbio.2015.08.042.
[40] Y.-H. Leem, K.-S. Lee, J.-H. Kim, H.-K. Seok, J.-S. Chang, D.-H. Lee, Magnesium ions facilitate integrin alpha 2- and alpha 3-mediated proliferation and enhance alkaline phosphatase expression and activity in hBMSCs, J. Tissue Eng. Regen. Med. (2014), https://doi.org/10.1002/term.1861.
[41] G.S. Stein, J.B. Lian, T.A. Owen, Relationship of cell growth to the regulation of tissue-specific gene expression during osteoblast differentiation, FASEB J. 4 (1990) 3111–3123, https://doi.org/10.1096/fasebj.4.13.2210157.